Torus Constraints in ANEPD-CXO245: A Compton-thick AGN with Double-peaked Narrow Lines

Takamitsu Miyaji[1] , Martín Herrera-Endoqui[1], Mirko Krumpe[2], Masaki Hanzawa[3], Ayano Shogaki[3], Shuji Matsuura[3] ,
Atsushi Tanimoto[4] , Yoshihiro Ueda[4] , Tsuyoshi Ishigaki[5], Laia Barrufet[6], Hermann Brunner[7], Hideo Matsuhara[8],
Tomotsugu Goto[9], Toshinobu Takagi[10], Chris Pearson[11,12] , Denis Burgarella[13], Nagisa Oi[14], Matthew Malkan[15] ,
Yoshiki Toba[4,16,17] , Glenn J. White[11,12] , and Hitoshi Hanami[5]

[1] Instituto de Astronomía sede Ensenada, Universidad Nacional Autónoma de México, Km 107, Carret. Tij.-Ens., Ensenada, 22060, BC, México
miyaji@astro.unam.mx
[2] Leibniz Institut für Astrophysik, Potsdam, An der Sternwarte 16, D-14482 Potsdam, Germany
[3] Department of Physics, Kwansei Gakuin University, 2-1 Gakuen, Sanda, Hyogo 669-1337, Japan
[4] Department of Astronomy, Kyoto University, Kitashirakawa-Oiwake-cho, Sakyo-ku, Kyoto 606-8502, Japan
[5] Department of Science and Technology, Iwate University, 3-18-34 Ueda, Morioka, Iwate 020-8550, Japan
[6] European Space Astronomy Center (ESAC), E-28691 Villanueva de la Canada, Spain
[7] Max-Planck-Institut für extraterrestrische Physik, D-85748 Garching bei München, Germany
[8] JAXA/ISAS, 3-1-1 Yoshinodai, Sagamihara, Kanagawa, Japan
[9] National Tsing Hua University, No. 101, Section 2, Kuang-Fu Road, Hsinchu 30013, Taiwan
[10] Japan Space Forum, 3-2-1, Kandasurugadai, Chiyoda-ku, Tokyo 101-0062, Japan
[11] RAL Space, STFC Rutherford Appleton Laboratory, Chilton, Didcot, Oxfordshire OX11 0QX, UK
[12] The Open University, Milton Keynes, MK7 6AA, UK
[13] Aix-Marseille Université, CNRS, LAM (Laboratoire d'Astrophysique de Marseille) UMR 7326, F-13388 Marseille, France
[14] Tokyo University of Science, 1-3 Kagurazaka, Shinjuku-ku, Tokyo 162-8601, Japan
[15] Department of Physics and Astronomy, UCLA, 475 Portola Plaza, Los Angeles, CA 90095-1547, USA
[16] Academia Sinica Institute of Astronomy and Astrophysics, 11F of Astronomy-Mathematics Building, AS/NTU, No.1, Section 4, Roosevelt Road, Taipei 10617,
Taiwan
[17] Research Center for Space and Cosmic Evolution, Ehime University, 2-5 Bunkyo-cho, Matsuyama, Ehime 790-8577, Japan

Abstract

We report on the torus constraints of the Compton-thick active galactic nucleus (AGN) with double-peaked optical narrow-line region emission lines, ANEPD-CXO245, at $z = 0.449$ in the *AKARI* NEP Deep Field. The unique infrared data on this field, including those from the nine-band photometry over 2–24 μm with the *AKARI* Infrared Camera, and the X-ray spectrum from *Chandra* allow us to constrain torus parameters such as the torus optical depth, X-ray absorbing column, torus angular width (σ), and viewing angle (i). We analyze the X-ray spectrum as well as the UV–optical–infrared spectral energy distribution (UOI-SED) with clumpy torus models in X-ray (XCLUMPY) and infrared (CLUMPY), respectively. From our current data, the constraints on σ–i from both X-rays and UOI show that the line of sight crosses the torus as expected for a type 2 AGN. We obtain a small X-ray scattering fraction ($<0.1\%$), which suggests narrow torus openings, giving preference to the bipolar outflow picture of the double-peaked profile. Comparing the optical depth of the torus from the UOI-SED and the absorbing column density N_{H} from the X-ray spectrum, we find that the gas-to-dust ratio is $\gtrsim 4$ times larger than the Galactic value.

Unified Astronomy Thesaurus concepts: Active galactic nuclei (16); X-ray active galactic nuclei (2035); Infrared galaxies (790); Infrared photometry (792); Spectroscopy (1558)

1. Introduction

In the course of our multiwavelength survey on the *AKARI* NEP Deep Field (ANEPD), including *Chandra* X-ray observations (Krumpe et al. 2015; Miyaji et al. 2017), optical spectroscopy (Shogaki 2018), and early UV–optical–infrared (UOI) spectral energy distribution (SED) analysis (Hanami et al. 2012), we have found an optically type 2 Compton-thick (CT) active galactic nucleus (AGN), ANEPD-CXO245 (hereafter CXO245; $z = 0.449$, $[\alpha, \delta]_{J2000} = [17^h56^m01\overset{s}{.}69, 66°35' 00\rlap{.}''6]$), which exhibits double-peaked optical emission lines from the AGN narrow-line region (NLR).

About $\sim 1\%$ of present-day type 2 AGNs show double-peaked NLR features (Liu et al. 2010). The origin of the double-peaked narrow lines can be heterogeneous and may be caused by dual AGNs, wind-driven outflows, radio-jet driven outflows, and rotating ring-like NLRs (Müller-Sánchez et al. 2015). To discriminate among these scenarios, AGN torus

parameters that can be obtained by the analysis of the X-ray spectrum and/or UV–optical–infrared spectral energy distribution (UOI-SED) can give a clue, in particular, to distinguish between the outflow and rotating NLR pictures. In the case of a narrow torus opening, it is more difficult for a rotating ring to cross the ionization cone, and the bipolar picture would be favorable. If the line of sight is almost perpendicular to the polar axis, the two sides of a bipolar outflow would show similar line-of-sight velocities, and in this case, the outflow picture would not be favored. In any case, whether the bipolar outflows and/or rotating rings are generally associated with highly absorbed CT-AGNs can have implications in their evolution stage. The CT-AGNs may be at the stage of starting feedback through outflows or tidally disrupted infalling clouds generating a ring-like structure.

Another interesting implication of X-ray spectral and UOI-SED analysis is the gas-to-dust ratio of the AGN torus, since

Table 1
UV–Optical–IR Photometry Used

Band	λ_{eff} (μm)	Flux (mJy)	Err.(1σ) (mJy)	Telescope/Instrument
NUV	0.229	4.980e−4	8.0e−5	*GALEX*
u^*	0.381	1.061e−3	1.8e−5	CFHT/MEGACAM
B	0.437	2.584e−3	8.8e−6	SUBARU/SCAM
V	0.545	7.553e−3	1.6e−5	SUBARU/SCAM
r	0.651	1.939e−2	1.9e−5	SUBARU/SCAM
NB711	0.712	2.547e−2	3.1e−5	SUBARU/SCAM
i	0.768	3.273e−2	2.3e−5	SUBARU/SCAM
z	0.919	4.526e−2	4.6e−5	SUBARU/SCAM
Y	1.03	7.973e−2	5.1e−4	CFHT/WIRCAM
J	1.25	1.113e−1	9.2e−4	CFHT/WIRCAM
Ks	2.15	1.886e−1	1.0e−3	CFHT/WIRCAM
N2	2.41	2.198e−1	3.1e−3	*AKARI*/IRC
N3	3.28	1.881e−1	2.2e−3	*AKARI*/IRC
N4	4.47	1.706e−1	2.0e−3	*AKARI*/IRC
S7	7.30	4.521e−1	1.4e−2	*AKARI*/IRC
S9W	9.22	7.238e−1	1.8e−2	*AKARI*/IRC
S11	10.9	1.036e+0	2.3e−2	*AKARI*/IRC
L15	16.2	1.562e+0	3.7e−2	*AKARI*/IRC
L18W	19.8	2.297e+0	4.0e−2	*AKARI*/IRC
L24	23.4	3.342e+0	8.6e−2	*AKARI*/IRC
PACS100	100	4.760e+0	1.5e+0	*HERSCHEL*/PACS
PACS160	160	1.768e+1	4.5e+0	*HERSCHEL*/PACS
PSW	250	2.974e+1	3.8e+0	*HERSCHEL*/SPIRE
PMW	350	2.353e+1	2.9e+0	*HERSCHEL*/SPIRE
PLW	500	1.320e+1	3.7e+0	*HERSCHEL*/SPIRE

the torus IR emission is from dust, whereas the X-ray absorption and reflection are produced by gas (Ogawa et al. 2019; Tanimoto et al. 2019).

In view of these, we conduct an AGN torus analysis of CXO245 both from our *Chandra* X-ray spectrum as well as the UOI-SED taking advantage of the unique mid-IR photometric bands available in ANEPD. In Section 2, we summarize the data set used. In Section 3, we summarize the key results from the optical emission lines and explain our methods and results of individual and joint X-ray spectral and UOI-SED analyses. Discussions and concluding remarks are made in Section 4.

We use $H_0 = 70$ km s^{-1} Mpc^{-1}, $\Omega_{\mathrm{m}} = 0.3$, and $\Omega_\Lambda = 0.7$ throughout this Letter.

2. Data

2.1. UV, Optical, and Infrared (UOI) Data

This object was found as a result of our *AKARI* survey on the North Ecliptic Pole (NEP) region (*AKARI* NEP Deep Field; e.g., Matsuhara et al. 2006), where deep observations with all nine bands of the InfraRed Camera (IRC; $\lambda_{\mathrm{eff}} = 2, 3, 4, 7, 9, 11, 15, 18,$ and $24\ \mu$m) were made. Extensive multiwavelength images have been obtained on this field by ground-based and space-borne observatories. We use UOI photometric measurements from the *Galaxy Evolution Explorer* (*GALEX*; Burgarella et al. 2019), Subaru Telescope Suprime Cam (SCAM; Murata et al. 2013), Canada–France–Hawaii Telescope (CFHT) MegaCam and WIRCAM (Oi et al. 2014), and *Herschel* PACS (Pearson et al. 2019)/SPIRE. The SPIRE data, originally published by Burgarella et al. (2019) has been reanalyzed by C. Pearson et al. (2019, in preparation), and we use the revised photometry. Table 1 shows a summary of the
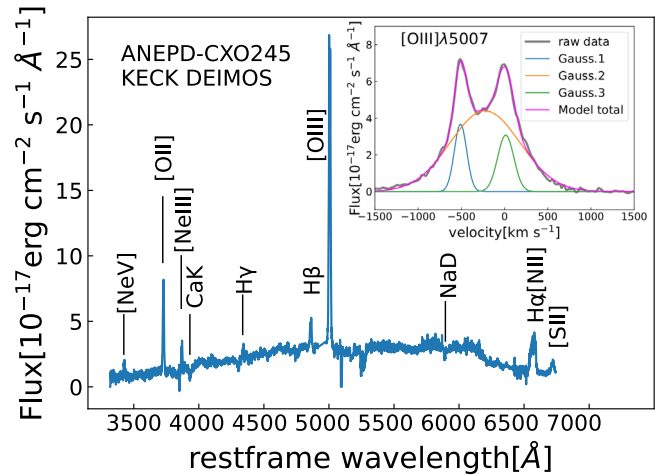
Figure 1. KECK DEIMOS spectrum of ANEPD-CXO245 from our 2011 run in rest frame. The inset shows the profile of the double-peaked [O III]λ5007 emission line from our 2008 spectrum in the radial velocity space with a three-Gaussian decomposition model. The raw data, model total, and each model component are drawn as labeled.

UOI photometry. The optical spectra of CXO245 have been obtained during our KECK (DEIMOS) runs in 2008 and 2011 and reduced by Shogaki (2018) using the DEIMOS DEEP2 reduction pipeline. The spectrum from the 2011 run is shown in Figure 1.

2.2. X-Ray Data and Reduction

A major fraction ($\sim$0.25 deg^2) of ANEPD has been observed with *Chandra* with a total exposure of $\sim$300 ks (Krumpe et al. 2015). CXO245 is covered by the *Chandra* ACIS-I fields of view of seven OBSIDs (see *Facilities*; total exposure $\sim$120 ks with off-axis angles from $3'\!.3$ to $9'\!.6$). The X-ray spectrum of each OBSID has been extracted from a circular region with a radius corresponding to the larger of 50% ECF at 3.5 keV (from the Ciao tool `psfsize_srcs`) or 3farcs5. The background spectrum is extracted from an annulus with inner and outer radii of $10''\!.5$ and $55''$, respectively, excluding a $10''$ region around another X-ray source (ANEPD-CXO358). A merged source and a background spectra have been generated using the Ciao tool combine_spectrum with the option `bscale_method=time`. This option generates both the combined source and background spectra in integer counts per bin accompanied by an appropriately weighted mean response matrix and a background scaling factor. These allow us to fit the background subtracted spectrum with full Poisson statistics (for small counts) with the XSPEC option `cstat`. In our X-ray spectroscopic analysis, we use the merged source spectrum with the supporting files created in this step. The resulting X-ray spectrum is shown in Figure 2(a) along with the model described in Section 3.2.1.

3. Analysis and Results

3.1. Optical Emission Lines

The fluxes of each emission line have been obtained with Gaussian+linear continuum fits. Multiple Gaussian components are used if needed. The details of the line spectral analysis is beyond the scope of this Letter. Here we describe the key results of the analysis.
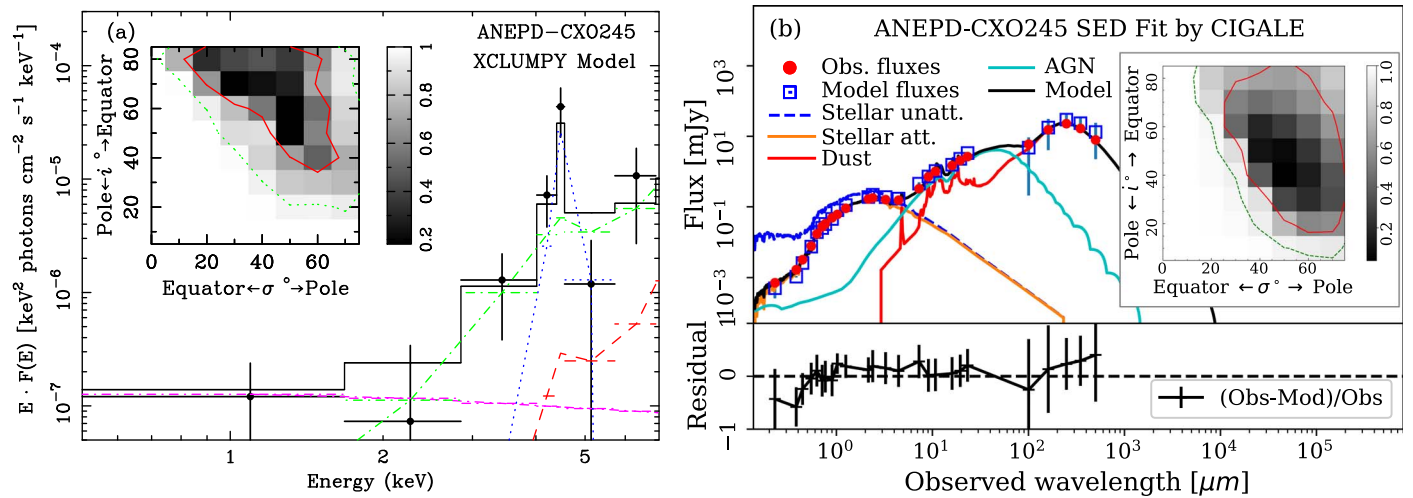
Figure 2. (a) Unfolded $E \cdot F(E)$ representation of our *Chandra* ACIS-I spectrum of ANEPD-CXO245. The black filled circles with error bars show the observed data binned to at least 2σ/bin up to 80 ACIS PI channels. The binning is for display only. The solid black histogram shows the best-fit model described in Section 3.2.1. Also plotted are the reflected continuum (green dotted–dashed line), reflected fluorescence line (blue dotted line), and transmitted (red dashed line) and scattered (magenta dotted–dotted–dashed line) components. The inserted box shows the integrated probability image and confidence contours in the σ–i space in grids of $10 \times 10 \ \mathrm{deg}^2$/pixel. The contours correspond to integrated marginal probabilities of 68% (red solid contour) and 95% (green dotted contour). (b) Optical–IR data fitted with CIGALE with the CLUMPY implementation. The photometry data and best-fit model with the contribution of each component are shown as labeled with residuals. The curve labeled "Dust" refers to the dust emission from star formation activity, while "AGN" refers to the AGN torus dust emission from CLUMPY. The inset shows the integral probability image and the confidence contours at the same levels as in panel (a).

1. The line ratios of [O III]$\lambda5007$/H$\beta \sim 10$ and [N II] $\lambda6583$/H$\alpha \sim 1.5$ are well inside the AGN regime in the BPT diagnostic diagram (Baldwin et al. 1981). The spectrum shows [Ne V]$\lambda3425$, which is an unambiguous indication of the AGN NLR.

2. The line profiles of the [O III]$\lambda5007$, Hβ, and Hα emission features are all well represented by two narrow (FWHM ~ 150 [km s^{-1}] each) and one broader (FWHM ~ 900 [km s^{-1}]) components. The profiles of noisier [Ne III]$\lambda3869$ and [Ne V]$\lambda3425$ lines also show similar double peaks. Figure 1 (inset) shows the line profile of [O III]$\lambda5007$ with the best-fit three-Gaussian components as the best example.

3. The two narrow components are separated by $\sim$500 km s^{-1} and have similar fluxes. The peak of the broad component is just halfway between the two narrower peaks.

4. The star formation dominated line [O II]$\lambda3727$ is single-peaked. Our nominal redshift ($z = 0.499$) is based on this line.

3.2. X-Ray Spectrum and IR SED: Torus Analysis

3.2.1. Clumpy Torus: X-Ray Spectrum

Current popular models of AGN tori involve dusty-gas media consisting of "clumps" (e.g., Elitzur & Shlosman 2006; Nenkova et al. 2008).

We first analyze the *Chandra* spectrum of CXO245 using the new X-ray Clumpy Torus model XCLUMPY (Tanimoto et al. 2019), which has the same geometry and geometrical parameters as the CLUMPY (Nenkova et al. 2008) model. Thus, direct comparisons with the results of Section 3.2.2 are possible. We use the XSPEC mode of the form

```
phabs * (zphabs * cabs * cutoffpl
    +const * cutoffpl
    +atable{xclumpy_R.fits}
    +atable{xclumpy_L.fits}).
```

The first phabs represents the Galactic absorption toward the source direction, and its column density is fixed to $N_{\mathrm{H,Gal}} = 4 \times 10^{20} \ \mathrm{cm}^{-2}$ (Kalberla et al. 2005). The first and second terms in the parenthesis are the transmitted and scattered primary continua, respectively. The former is subject to a line-of-sight photoelectric absorption (zphabs) and a Compton scattering (cabs) through the torus. The latter expresses that the fraction $f_{\mathrm{X,sct}}$ (represented by const) is scattered by electrons in thin plasma above and below the polar torus openings. The XSPEC table models xclumpy_R.fits and xclumpy_L.fits provide the continuum and the emission line (including fluorescent emission lines from elements up to $Z = 30$, dominated by Fe Kα) components of the X-ray reflection from the clumpy torus, respectively. The normalization and photon indices of the primary X-ray continuum are free parameters, where the latter is allowed to vary within $1.5 \leqslant \Gamma \leqslant 2.5$, while its cutoff energy is fixed to $E_c = 300 \ \mathrm{keV}$ (Koss et al. 2017; Ricci et al. 2018). These parameters are common to the reprocessed, transmitted, and scattered components. The solar abundance (Anders & Grevesse 1989) is assumed. The redshift parameters of the model components that require one are fixed to $z = 0.449$. Spectral fits are made in channel energies of 0.5–7.0 keV using a Markov Chain Monte Carlo (MCMC) chain with a length of 40,000 (using XSPEC's chain command). In the current version of XCLUMPY, the number of clumps along the equator, the ratio of the outer to inner radii, and the radial clumpy distribution index are fixed to $N_{\mathrm{clump}}^{\mathrm{Equ}} = 10$, $Y = 20$, and $q = 0.5$, respectively. The parameter ranges covered by the model implementation for the equatorial column density, torus width, and viewing angle are $23 \leqslant \log N_{\mathrm{H}}^{\mathrm{Equ}} \leqslant 26$, $10° \leqslant \sigma \leqslant 70°$, and $20° \leqslant i \leqslant 87°$, respectively.

Table 2 shows the best-fit parameters and the 90% confidence ranges obtained from the MCMC chain. Figure 2(a) shows the best-fit model and the contribution of various components with the unfolded ACIS spectrum. Figure 2(a) (inset) shows the integrated probability grayscale

Table 2
Model Parameters[a]

Param.	X-Ray Spectrum	UOI-SED	Joint
$\log N_{\mathrm{H}}^{\mathrm{Equ}}$ [b]	24.7 (24.5; 25.9[*])	...	...
$\tau_{\mathrm{V}} N_0$ [c]	...	400(400; 400)	...
σ [d]	55 (18; 69[*])	50 (20[*]; 70[*])	50 (20[*]; 70[*])
i [e]	49 (30; 85[*])	40 (20; 90[*])	50 (30; 80[*])
Γ [f]	2.2 (1.5; 2.4)	...	...
$\log f_{\mathrm{X,sct}}$ [g]	−4.0 (−6.0[*]; −3.0)	...	...
$f_{X,15}$ [h]	8 (5; 9)	...	...
$\log L_{\mathrm{X}}^{\mathrm{int}}$ [i]	44.7 (44.4; 45.7)	...	...
$\log L_{\mathrm{AGN}}^{\mathrm{IR}}$ [j]	...	44.6 (44.5; 44.8)	...
$f_{\mathrm{AGN}}^{\mathrm{IR}}$ [k]	...	0.5 (0.5; 0.6)	...

Notes.
[a] Best-fit values with 90% confidence range in one parameter in the parentheses. The bounds that are pegged at model limits are marked with an asterisk ([*]).
[b] Torus column density cm^{-2} at the equator.
[c] Total optical depth of clumps through the equator at $\lambda = 0.55\,\mu$m.
[d] Torus angular width in degrees.
[e] Viewing angle from the pole in degrees.
[f] Photon index of the primary X-ray continuum.
[g] X-ray scattering fraction.
[h] X-ray (0.5–7 keV) flux in 10^{-15} erg s^{-1} cm^{-2} from the best-fit model.
[i] Intrinsic rest frame 2–10 keV luminosity in erg s^{-1} of the primary X-ray continuum.
[j] Infrared luminosity in erg s^{-1} from the AGN torus.
[k] $f_{\mathrm{AGN}} = L_{\mathrm{IR}}^{\mathrm{AGN}}/(L_{\mathrm{IR}}^{\mathrm{SF}} + L_{\mathrm{IR}}^{\mathrm{AGN}})$, where $L_{\mathrm{IR}}^{\mathrm{SF}}$ is the dust IR luminosity from star formation.

image and its contours (see the caption) in the σ–i space. Because the available solid angle per viewing angle (i) is proportional to $\sin i$, we use $\sin i$ as a prior. Practically, we calculate the 90% ranges from the chain points weighted by the prior. Likewise, we calculate the marginal probability in each bin $P_{\mathrm{X}}(\sigma_j, i_k)$ by accumulating the weighted chain points and normalizing. The integrated probability $I_{\mathrm{X}}(\sigma_j, i_k)$ is obtained by iterating, in the order of decreasing $P_{\mathrm{X}}(\sigma_j, i_k)$:

$$I_{\mathrm{X}}(\sigma_j, i_k) = P_{\mathrm{X}}(\sigma_j, i_k) + I_{\mathrm{X,prev}}, \qquad (1)$$

where $I_{\mathrm{X,prev}}$ is the integrated probability from the previous step (or 0 in the first step).

The spectrum shows a strong Fe Kα line characteristic of a CT-AGN. The derived column densities (both equatorial and line of sight) correspond to $N_{\mathrm{H}} > 10^{24}$ cm^{-2} and thus CXO245 can be classified as a CT-AGN. The confidence contours of Figure 2 and Table 2 show that the line-of-sight viewing angle cannot be too close to the pole ($i > 30°$; 90% lower limit).

3.2.2. Clumpy Torus: UOI-SED

We also investigate the AGN torus constraints from the UOI-SED ($\approx$0.2–1000 μm) of CXO245 in the framework of the clumpy torus model CLUMPY (Nenkova et al. 2008). For this purpose, we have made a modification to the CIGALE package (Noll et al. 2009; Boquien et al. 2019) to include an implementation of CLUMPY. To make the analysis consistent with the XCLUMPY X-ray spectrum, we search for best-fit parameters assuming $N_0 = 10$, $Y = 20$, and $q = 0.5$. In the SED fit, we use the galaxy stellar component (Bruzual & Charlot 2003) with a Salpeter (1955) initial mass function, double exponentially decaying star formation history, and an

attenuation by Charlot & Fall (2000). For the dust emission models, we use the Dale et al. (2014) model for the star formation and CLUMPY for the AGN torus. The optical part is included in the fits, because the star formation dust component in the IR and the dust attenuation of the starlight are energetically connected. This helps make a better separation of the AGN and star formation IR components.

There are certain limitations in the best-fit and parameter error search in CIGALE. For table models, CIGALE only allows us to evaluate χ^2 at the grid points in the table, and no interpolations are made, unlike the X-ray spectral analysis using XSPEC. The MCMC is not implemented either. Thus, the best-fit values and bounds are among these grid points. In our implementation, the grids of the free geometrical parameters are $\sigma = 20°$–$70°$ and $i = 0°$–$90°$ in every $10°$, respectively. A common approach in determining a 90% confidence error range is to use the $\Delta\chi^2 < 2.7$ criterion. However, especially for σ and i, parameters are often pegged at the model limits, and therefore this criterion does not properly indicate the true 90% probability range. Thus, we determine the 90% confidence range ($p-$; $p+$) of the parameter p by $C(<p-) \sim 0.05$ and $C(<p+) \sim 0.95$, respectively, where C is the cumulative probability:

$$C(<p) = \frac{\sum_{p_k \leqslant p} \sin i_k \exp[-\chi^2(p_k)/2]}{\sum_{\mathrm{all}\,k} \sin i_k \exp[-\chi^2(p_k)/2]}. \qquad (2)$$

Due to computational limitations, we take $\chi^2(p_i)$ as the minimum value at $p = p_i$ where all other parameters are allowed to vary, rather than the marginal probability, and i_k is the best-fit viewing angle when p is fixed to p_k. The 90% confidence ranges are approximate because of the discreteness of the parameter grid.

Likewise, the probability at each point of the two-parameter space (σ_j, i_k) is determined by

$$P_{\mathrm{UOI}}(\sigma_j, i_k) = \frac{\sin i_k \exp[-\chi^2(\sigma_j, i_k)/2]}{\sum_{j'k'} \sin i_{k'} \exp[-\chi^2(\sigma_{j'}, i_{k'})/2]}, \qquad (3)$$

where $\chi^2(\sigma_j, i_k)$ is the minimum χ^2 value at $(\sigma, i) = (\sigma_j, i_k)$ with respect to all other parameters. The sum in the denominator is for all the grid points in (σ, i). Then the integrated probability $I_{\mathrm{UOI}}(\sigma_j, i_k)$ is obtained in the same manner as Equation (1). The resulting best-fit parameters and the 90% confidence ranges in one parameter for the AGN torus are shown in Table 2. Figure 2(b)(inset) shows the integrated probability grayscale image in the grids mentioned above with contours.

3.2.3. X-Ray–UOI Joint Torus Constraints

The X-ray spectrum and UOI-SED give independent probes of the torus parameters. The *AKARI* IRC and *Chandra* observations were made during 2006 and 2010–2011, respectively, and we do not expect significant changes in the torus properties between these observations. Thus we also explore the joint constraints of the torus parameters. In the current implementation, the parameters that are common to both XCLUMPY and CLUMPY are σ and i. The joint probability
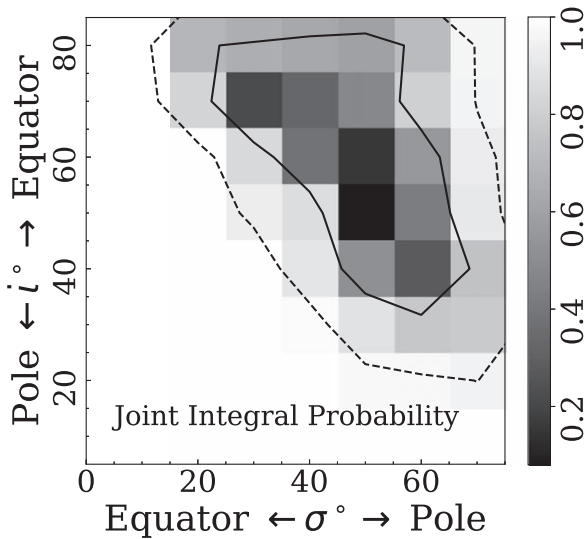
Figure 3. Integrated probability in the σ–i space from the joint X-ray and UOI analysis. The solid and dashed contours represent 68% and 95% ranges for the two parameters, respectively.

map is calculated by

$$P_{\text{Joint}}(\sigma_j, i_k) = \frac{P_{\text{X}}(\sigma_j, i_k) P_{\text{UOI}}(\sigma_j, i_k)}{\sum_{j'k'} P_{\text{X}}(\sigma_{j'}, i_{k'}) P_{\text{UOI}}(\sigma_{j'}, i_{k'})}, \qquad (4)$$

where the sum is over all pixels in the (σ, i) space. The integrated joint probability image I_{Joint} is calculated from P_{Joint} in the same manner as Equation (1), and is shown in Figure 3.

We note that the new results by A. Tanimoto et al. (2019, in preparation) on the X-ray and IR clumpy torus analyses of a sample of 10 nearby type 2 AGNs show inconsistencies of σ and i values between those obtained by X-ray and IR in some objects. Thus the results of the joint constraints should be used with caution.

4. Discussion and Concluding Remark

The developments of modern AGN torus models, both in the infrared and X-rays, have opened up the possibility of constraining its geometric parameters such as the torus angular width and the viewing angle, in addition to the optical depth (UOI) and the X-ray absorption column density.

In our UOI data set, $\log L_{\text{AGN}}^{\text{IR}}$ and $\tau_V N_0$ are well constrained. We verify that $\log L_{\text{AGN}}^{\text{IR}}$ changes very little when we use other models of torus and the star formation dust components (Fritz et al. 2006; Schreiber et al. 2016). With CLUMPY, we find $\tau_V N_0 = 400$ as the best fit among the model's grid points, and the neighboring grid values of 200 and 600 are strongly excluded. In the X-ray analysis, we obtain $N_{\text{H}}^{\text{Equ}} \gtrsim 4 \times 10^{24}$ cm^{-2}, where the upper bound is unconstrained. Thus, we obtain $N_{\text{H}}^{\text{Equ}}/A_V^{Eq} \gtrsim 3 \times 10^{21}$ cm^{-2} mag^{-1} ($A_V = 2.5\tau_V N_0/\ln(10)$). The comparison of this ratio with the Galactic value ($N_{\text{H}}/A_V = 1.87 \times 10^{21}$ cm^{-2} mag^{-1}; Draine 2003) implies that the gas-to-dust ratio of the CXO245 torus is at least four times larger than that of the galaxy. This is consistent with the results from some other works. Tanimoto et al. (2019) have found a gas-to-dust ratio of ~26 times the Galactic value for the nearby CT-AGN the Circinus galaxy. New results from a systematic study of 10 additional nearby Seyfert 2 galaxies with XCLUMPY and CLUMPY (A. Tanimoto et al. 2019, in preparation) include measurements of two other CT-AGNs, one of which shows a

larger N_{H}/A_V value than the Galactic one. The comparison of the silicate absorption depth $\tau_{9.7}$ at 9.7 μm and N_{H} by González-Martín et al. (2013) shows systematically higher N_{H} than expected from $\tau_{9.7}$ expected from the Galatctic gas-to-dust ratio for obscured AGNs.

The constraints on σ and i are much looser. There are, however, some meaningful constraints. The X-ray analysis strongly excludes $90° - i \gtrsim \sigma$, meaning that the line of sight crosses the torus material, as expected for type 2 AGNs. We also obtain a lower limit to the viewing angle ($i > 30°$), excluding a line of sight that is close to the polar axis. The UOI-SED analysis shows a similar trend.

One of our original motivations of this work was to obtain constraints of these angles to give clues to discriminate between the bipolar outflow and a rotating ring origin of the double-peaked NLR lines (Section 1). In the constraints of i and σ themselves, neither the X-ray spectrum nor UOI-SED can suggest which picture is preferred. On the other hand, the very small scattering fraction ($f_X \lesssim 0.1\%$) from our X-ray spectral analysis suggests a small opening angle (large σ). While the f_X–σ relation has not yet been calibrated (Ueda et al. 2007; Yamada et al. 2019), the rather small scattering fraction suggests some preference to the bipolar outflow picture.

The nine-band photometric data with *AKARI* IRC available in the *AKARI* NEP Deep and Wide fields have made torus analyses with the UOI-SED fit possible for CT-AGNs across a wide redshift range. These can then be compared and/or combined with the X-ray torus analysis, as demonstrated in this Letter. By the analyses on both sides, we obtain a constraint on the gas-to-dust ratio of the AGN torus and loose constraints on the torus width and viewing angles. We are planning to extend this work to the ~5.4 deg^2 *AKARI* NEP Wide Field by combining the *AKARI* IRC and supporting UOI data and the scheduled deep exposures with the recently launched *eROSITA/ART-XC* (Merloni et al. 2012; Pavlinsky et al. 2018) in the NEP region. That would provide the candidates for further *Chandra*, *XMM-Newton*, and *JWST*, and, on a longer timescale, *Athena* observations.

ORCID iDs

Takamitsu Miyaji ⬤ https://orcid.org/0000-0002-7562-485X
Shuji Matsuura ⬤ https://orcid.org/0000-0002-5698-9634
Atsushi Tanimoto ⬤ https://orcid.org/0000-0002-0114-5581

Yoshihiro Ueda https://orcid.org/0000-0001-7821-6715
Chris Pearson https://orcid.org/0000-0001-6139-649X
Matthew Malkan https://orcid.org/0000-0001-6919-1237
Yoshiki Toba https://orcid.org/0000-0002-3531-7863
Glenn J. White https://orcid.org/0000-0002-7126-691X

References

Anders, E., & Grevesse, N. 1989, GeCoA, 53, 197
Baldwin, J. A., Phillips, M. M., & Terlevich, R. 1981, PASP, 93, 5
Boquien, M., Burgarella, D., Roehlly, Y., et al. 2019, A&A, 622, A103
Bruzual, G., & Charlot, S. 2003, MNRAS, 344, 1000
Burgarella, D., Mazyed, F., Oi, N., et al. 2019, PASJ, 71, 12
Charlot, S., & Fall, S. M. 2000, ApJ, 539, 718
Dale, D. A., Helou, G., Magdis, G. E., et al. 2014, ApJ, 784, 83
Draine, B. T. 2003, ARA&A, 41, 241
Elitzur, M., & Shlosman, I. 2006, ApJL, 648, L101
Fritz, J., Franceschini, A., & Hatziminaoglou, E. 2006, MNRAS, 366, 767
González-Martín, O., Rodríguez-Espinosa, J. M., Díaz-Santos, T., et al. 2013, A&A, 553, A35
Hanami, H., Ishigaki, T., Fujishiro, N., et al. 2012, PASJ, 64, 70

Kalberla, P. M. W., Burton, W. B., Hartmann, D., et al. 2005, A&A, 440, 775
Koss, M., Trakhtenbrot, B., Ricci, C., et al. 2017, ApJ, 850, 74
Krumpe, M., Miyaji, T., Brunner, H., et al. 2015, MNRAS, 446, 911, (K15)
Liu, X., Shen, Y., Strauss, M. A., & Greene, J. E. 2010, ApJ, 708, 427
Matsuhara, H., Wada, T., Matsuura, S., et al. 2006, PASJ, 58, 673
Merloni, A., Predehl, P., Becker, W., et al. 2012, arXiv:1209.3114
Miyaji, T., Krumpe, M., Brunner, H., et al. 2017, PKAS, 32, 235
Müller-Sánchez, F., Comerford, J. M., Nevin, R., et al. 2015, ApJ, 813, 103
Murata, K., Matsuhara, H., Wada, T., et al. 2013, A&A, 559, A132
Nenkova, M., Sirocky, M. M., Ivezić, Ž., et al. 2008, ApJ, 685, 147
Noll, S., Burgarella, D., Giovannoli, E., et al. 2009, A&A, 507, 1793
Ogawa, S., Ueda, Y., Yamada, S., et al. 2019, ApJ, 875, 115
Oi, N., Matsuhara, H., Murata, K., et al. 2014, A&A, 566, A60
Pavlinsky, M., Levin, V., Akimov, V., et al. 2018, Proc. SPIE, 10699, 106991Y
Pearson, C., Barrufet, L., Campos Varillas, M. d. C., et al. 2019, PASJ, 71, 13
Ricci, C., Ho, L. C., Fabian, A. C., et al. 2018, MNRAS, 480, 1819
Salpeter, E. E. 1955, ApJ, 121, 161
Schreiber, C., Elbaz, D., Pannella, M., et al. 2016, A&A, 589, A35
Shogaki, A. 2018, Master thesis, Kwansei Gakuin Univ. (in Japanese)
Tanimoto, A., Ueda, Y., Odaka, H., et al. 2019, ApJ, 877, 95
Ueda, Y., Eguchi, S., Terashima, Y., et al. 2007, ApJL, 664, L79
Yamada, S., Ueda, Y., Tanimoto, A., et al. 2019, ApJ, 876, 96